Soft Matter

PAPER

View Article Online
View Journal | View Issue

Cite this: *Soft Matter*, 2016, 12, 3461

Shear-induced amyloid fibrillization: the role of inertia†

Samantha A. McBride,[a] Sean P. Sanford,[b] Juan M. Lopez[c] and Amir H. Hirsa*[da]

Received 1st December 2015,
Accepted 28th February 2016

DOI: 10.1039/c5sm02916c

www.rsc.org/softmatter

Agitation of protein is known to induce deleterious effects on protein stability and structure, with extreme agitation sometimes resulting in complete aggregation into amyloid fibrils. Many mechanisms have been proposed to explain how protein becomes unstable when subjected to flow, including alignment of protein species, shear-induced unfolding, simple mixing, or fragmentation of existing fibrils to create new seeds. Here a shearing flow was imposed on a solution of monomeric human insulin *via* a rotating Couette device with a small hydrophobic fluid interface. The results indicate that even very low levels of shear are capable of accelerating amyloid fibril formation. Simulations of the flow suggest that the shear enhances fibrillization kinetics when flow inertia is non-negligible and the resulting meridional circulation allows for advection of bulk protein to the hydrophobic interface.

1 Introduction

Amyloidogenesis is a widely studied phenomenon because of the neurotoxicity of amyloid fibrils and because amyloid species are thought to be causational in a variety of proteopathic disorders.[1,2] These distinct protein aggregates form *via* templated growth from nucleation seeds into long, thin fibers. The final structure of amyloidogenic species is highly dependent on the nature of the seed and on the conditions of formation.[3] Many proteins of widely varying sizes and conformations are known to form crystalline amyloid structures upon exposure to perturbative factors such as high temperature or agitation.[3,4]

The reason that such a diverse range of proteins undergo amyloidogenesis is thought to be due to the nature of protein sequences. Protein folding occurs spontaneously as a result of a pattern of amino residues that vary in their relative hydrophobicities. Strongly hydrophobic groups fold towards the interior of the protein while more hydrophilic groups typically reside in outer portions.[5] A protein's three-dimensional structure results in its functionality *in vivo*, yet the pattern of greater and lesser hydrophobic regions that gives it structure also makes it susceptible to fibrillization.[6]

The generic pathway of fibril formation yields a sigmoidal curve when the native soluble protein concentration is plotted against time.[7] Initially there is a lag phase in which the soluble protein concentration remains relatively steady. Once a certain amount of protein has become destabilized due to some perturbation, such as heat or pressure, these unstable species unfold and combine with other protein monomers to form nucleation seeds. The soluble concentration begins to decrease rapidly in this growth phase as protein molecules come into contact with the seeds and assemble into amyloid fibrils. After a period of time a majority of native proteins have been amalgamated into the fibrils, and the transition phase levels off.[8]

It is well established that fluid agitation can expedite the transition of soluble protein into amyloid fibrils,[9] and experimental evidence suggests that shearing flows are responsible for the agitation-induced kinetic increase.[10] The mechanism by which shear acts upon native, soluble protein remains controversial. There are many hypotheses for why amyloid formation is enhanced by agitation. It has been suggested that shearing flow partially unfolds or degrades protein monomers.[11] However, the shear rates required for even partial unfolding are much greater than the shear rates that have been demonstrated to result in an increase in fibrillization.[10,12,13]

Pre-existing fibrils have been shown to be degraded by exposure to shear, suggesting another pathway for flow-induced fibrillization. There is experimental evidence that fragmentation resulting from agitation likely plays a role in increasing the rate of fibril growth, as fragmented fibrils serve as nucleation sites that cause other protein monomers to become unstable.[11,14,15] However, fragmentation does not explain the shear-induced increase observed in the nucleation and lag phases of amyloid formation.[15] There is also evidence suggesting that the onset of shear flow is the key to enhancement in the formation rate, and that the duration of shear is of lesser importance.[16]

[a] *Department of Chemical Engineering, Rensselaer Polytechnic Institute, Troy, NY, 12180-3590, USA*
[b] *Department of Biomedical Engineering, Rensselaer Polytechnic Institute, Troy, NY, 12180-3590, USA*
[c] *School of Mathematical and Statistical Sciences, Arizona State Univ., Tempe, AZ, 85287, USA*
[d] *Department of Mechanical, Aerospace and Nuclear Engineering, Rensselaer Polytechnic Institute, Troy, NY 12180-3590, USA. E-mail: hirsaa@rpi.edu*

† Electronic supplementary information (ESI) available. See DOI: 10.1039/c5sm02916c

There is also strong evidence indicating that the formation of fibrils under shear flows is dependent on the presence of a hydrophobic interface.[17] Amyloid species and precursors are highly surface active and will accumulate at hydrophobic interfaces.[18] For example, the beta sheet structures associated with amyloid fibrils form at the air–water interface at a rate of about 1500 times faster than they do in the bulk.[18] Indeed, removal of all hydrophobic interfaces completely eliminates fibrillization under some conditions.[17,18] Agitated fibrillization experiments in the presence of either an air–water or a Teflon–water interface demonstrated that fibrillization kinetics are proportional to the surface area of hydrophobic interfaces, while control experiments using glass boundaries showed no increased kinetics.[17] These results suggest that the mechanism behind agitation-induced fibrillization is dominated by reactions at hydrophobic interfaces. The association with hydrophobic interfaces is supported by simulations, which indicate that anchored protein is much more likely to denature under a shear field than protein in the bulk.[13]

While shear has a proven ability to induce amyloid fibrillization, it is also clear that extensional forces on protein molecules are not sufficient for even partial unfolding.[10,12,13] Given that destabilization and unfolding of monomers is thought to be a prerequisite for fibril formation, the mechanism of shear-induced fibrillization remains unknown. Here, the mechanism was investigated by subjecting solutions of insulin to shear using a rotating Couette device with a small hydrophobic interface. The Couette geometry with a stationary inner cylinder (Fig. 1) was chosen primarily because of its extreme stability. It is well established that the flow can be driven to very high rotation rates before any hydrodynamic instability is manifested. In the idealized situation, with infinitely long cylinders, the flow is only in the azimuthal direction and there is no secondary (meridional) flow.[19] However, the reality is that any experiment has to use finite length cylinders. The presence of endwalls, regardless of how far apart they are or whether they are stationary or rotating, always drives a secondary flow. If inertia is not negligible the secondary flow drives the radial distribution of shear away from uniform. The temptation is to use the analytical result for the idealized case rather than solving the Navier–Stokes equations for the boundary conditions used in the actual experiments. The simple analytic uni-directional (azimuthal) flow captures the primary flow quite well, however, in some situations inertia and the secondary flow (which are neglected) have far reaching consequences, as is the case in the experiments presented here.

We present experimental results on fibrillization kinetics over a wide range of shear in order to study in detail the effects of shearing flow. The apparatus used in these experiments was constructed of glass, which is hydrophilic. The flow geometry also included a free hydrophobic surface, constituting about 10% of the surface area. The free surface was covered with mineral oil, which provided the hydrophobic interface and prevented evaporation (which would have impacted protein concentration in an uncontrollable way). It also permitted the sampling of the bulk fluid with ease and minimal interference to the flow. Finally, because the oil film was thin, its effect on the flow of the protein solution could be computed readily without the need to simultaneously solve for the flow field in the oil domain. The experimental results demonstrate the influence of flow on the fibrillization process. The numerical simulations clarify the role of nonlinearity, associated with flow inertia and secondary flow, in fibrillization.

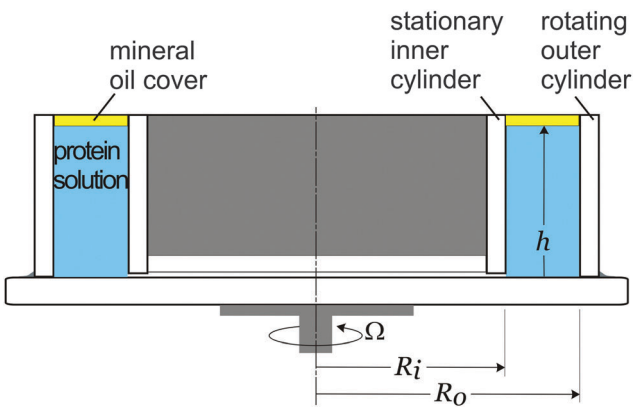

Fig. 1 Schematic of the rotating Couette flow device.

2 Materials and methods

2.1 Experimental methods

2.1.1 Flow device. The rotating Couette apparatus, depicted in Fig. 1, consists of a stationary inner cylinder of radius R_i = 2.22 cm, an outer cylinder of radius R_o = 2.50 cm that rotates at Ω [rad s^{-1}], with the bottom attached to the rotating outer cylinder. The gap between the rotating bottom and the stationary inner cylinder was less than 0.01 cm. The cylinders were constructed from precision bore borosilicate glass, and had a height of 1.1 cm. The flow apparatus was filled with protein solution to a height h = 0.9 cm, and then covered with a thin layer of mineral oil. The system was designed for easy disassembly and cleaning between experiments. Synchronous motors were used to spin the outer cylinder and the bottom at a constant angular velocity. Solution samples were withdrawn from approximately the mid-height. The experiments were conducted at an elevated temperature of 65 °C to increase fibrillization rates without the use of seeding.

2.1.2 Protein preparation. Recombinant human insulin was purchased from Sigma-Aldrich (91077C). Insulin was dissolved in de-ionized water at pH 1.6 (0.025 M HCl) containing 0.1 M NaCl. The low pH allows insulin to be monomeric, which is the form that fibrillization is thought to initiate from.[20] After solvation of insulin, the solution was filtered twice through a 0.2 μm syringe filter followed by pH cycling to maximize purity and homogeneity. Previous work has shown that filtration combined with pH cycling decreases variability between fibrillization experiments.[14] Experiments were performed at a nominal insulin concentration of 1 mg mL^{-1} after filtration. All experimental trials were repeated in triplicate to reduce

uncertainties and to generate error bars. The purity of the prepared protein solutions was established *via* mass spectrometry (see the figures in the ESI†)

2.1.3 Protein analysis measurements. It is well-established that insulin aggregates under the given buffer conditions (pH 1.6, 65 °C) are fibrillar.[3] A previous investigation using the Couette device described here, operating under the same buffer conditions, established the formation of amyloid fibrils using circular dichroism (demonstrating the depletion of alpha helix structures and the formation of beta sheet structures), atomic force microscopy (AFM) images, and thioflavin-T (ThT) fluorescence.[21] For the present study, these methods were not employed because of the additional disturbances they would have imposed on the flow. Instead, in order to limit the amount of solution withdrawn at each time point, kinetics were measured *via* the loss of the monomeric insulin concentration. In Fig. 2 we present an AFM image of insulin fibrils formed under shear in the Couette device, for illustrative purposes.

Aliquots of 20 μL were removed from the Couette flow device at specified times throughout the fibrillization experiments and placed in 0.2 mL PCR tubes. The tubes were centrifuged, at either 3000*g* or 50 000*g* for 10 minutes, to remove any aggregated protein prior to absorbance measurements. Independent experiments have confirmed that the two centrifugation rates gave consistent results.[15] Duplicate aliquots were analyzed from each tube. Soluble insulin concentration was measured using a plate reader (BioTek) that detects absorbance at 280 nm and 260 nm. Gen5 data analysis software was then used to calculate the concentration of soluble protein from the absorbance measurements.

2.2 Flow simulations

The continuum flow field in the rotating Couette device is governed by the Navier–Stokes equations coupled with a tangential stress balance at the oil–water interface and with no-slip boundary conditions of the stationary inner cylinder, and the rotating bottom and outer cylinder. The Navier–Stokes description of the bulk flow with a constant kinematic viscosity, ν [cm^2 s^{-1}], is a reasonable model until the solution has undergone significant fibrillization. The initial kinematic viscosity of the protein solutions at the operating temperature of 65 °C for all the experiments was 0.0044 cm^2 s^{-1}. Independent measurements of viscosity show that large departures (>20%) from the initial viscosity do not occur until significant fibrillization (50%) has occurred.

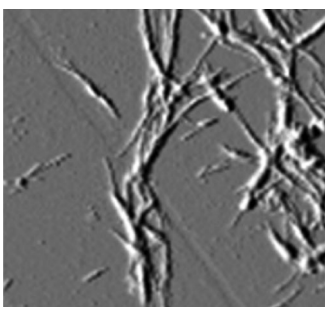

Fig. 2 Atomic force microscopy image (2 μm × 2 μm) of fibrils of human insulin produced in the Couette device with the outer cylinder rotating at 75 rad s^{-1}.

The system is non-dimensionalized using the gap between the cylinders, $d = (R_o - R_i)$ [cm], as the length scale, and $1/\Omega$ [s] as the time scale. For the entire range of conditions considered in this study, the flow remains axisymmetric. The axisymmetric flow is described using the streamfunction–vorticity formulation, where the non-dimensional velocity in cylindrical coordinates (r, θ, z) is

$$(u, v, w) = \left(-\frac{1}{r}\frac{\partial\psi}{\partial z}, v, \frac{1}{r}\frac{\partial\psi}{\partial r}\right), \quad (1)$$

where ψ is the streamfunction, and the corresponding vorticity is

$$\left(-\frac{1}{r}\frac{\partial(rv)}{\partial z}, \eta, \frac{1}{r}\frac{\partial(rv)}{\partial r}\right), \quad (2)$$

where the azimuthal component of vorticity η is

$$\eta = \frac{\partial u}{\partial z} - \frac{\partial w}{\partial r} = -\frac{1}{r}\left(\frac{\partial^2\psi}{\partial z^2} + \frac{\partial^2\psi}{\partial r^2} - \frac{1}{r}\frac{\partial\psi}{\partial r}\right). \quad (3)$$

In the streamfunction–vorticity formulation, the non-dimensional Navier–Stokes equations are

$$\frac{\partial v}{\partial t} + \frac{1}{r}\frac{\partial\psi}{\partial r}\frac{\partial v}{\partial z} - \frac{1}{r}\frac{\partial\psi}{\partial z}\frac{\partial v}{\partial r} - \frac{v}{r^2}\frac{\partial\psi}{\partial z} = \frac{1}{\mathrm{Re}}\left(\frac{\partial^2 v}{\partial z^2} + \frac{\partial^2 v}{\partial r^2} + \frac{1}{r}\frac{\partial v}{\partial r} - \frac{v}{r^2}\right), \quad (4)$$

$$\frac{\partial\eta}{\partial t} - \frac{1}{r}\frac{\partial\psi}{\partial z}\frac{\partial\eta}{\partial r} + \frac{1}{r}\frac{\partial\psi}{\partial r}\frac{\partial\eta}{\partial z} + \frac{\eta}{r^2}\frac{\partial\psi}{\partial z} - \frac{2v}{r}\frac{\partial v}{\partial z} = \frac{1}{\mathrm{Re}}\left(\frac{\partial^2\eta}{\partial z^2} + \frac{\partial^2\eta}{\partial r^2} + \frac{1}{r}\frac{\partial\eta}{\partial r} - \frac{\eta}{r^2}\right), \quad (5)$$

where $\mathrm{Re} = \Omega R_o d/\nu$ is the Reynolds number.

The boundary conditions are:

$$\text{stationary inner cylinder, } r = r_i: \quad (u, v, w) = (0, 0, 0), \quad (6)$$

$$\text{rotating outer cylinder, } r = r_o: \quad (u, v, w) = (0, 1, 0), \quad (7)$$

$$\text{rotating bottom, } z = 0: \quad (u, v, w) = (0, r/r_o, 0), \quad (8)$$

where r_i and r_o are the non-dimensional radii of the inner and outer cylinders. The boundary condition for the top was that of a highly viscous interface, for which the axial and radial velocity components vanish, *i.e.* $u = w = 0$, and the tangential stress balance at the interface, $z = h/d$, reduces to

$$\frac{\partial^2 v}{\partial r^2} + \frac{1}{r}\frac{\partial v}{\partial r} - \frac{v}{r^2} = 0. \quad (9)$$

The solution of (9), with boundary conditions $v(r_i,h/d) = 0$ and $v(r_o,h/d) = 1$, is

$$v(r,h/d) = Ar + B/r, \quad (10)$$

where $A = 1/\varepsilon$, $B = -A\varepsilon^2/(\varepsilon^2 - 1)^2$, and $\varepsilon = r_i/r_o$.

A useful quantity to characterize the flow is the shear

$$S = r\frac{\partial}{\partial r}\left(\frac{v}{r}\right). \quad (11)$$

The numerical technique used for this system is the same as that detailed in the study of Young *et al.* (2015).[22]

3 Results

3.1 Protein kinetics

Experimental assays of soluble insulin concentration plotted as a function of time were fitted to a sigmoidal model that is commonly used for describing fibrillization kinetics.[3] In this sigmoidal model the concentration of soluble protein, C [mg mL^{-1}], is given as a function of the initial concentration, C_0 [mg mL^{-1}], and time, t [h], by

$$C/C_0 = 1 + [1 + \exp(\kappa\, t_{1/2})]^{-1} - [1 + \exp(\kappa\,(t_{1/2} - t))]^{-1}, \quad (12)$$

where $t_{1/2}$ [h] is the half-time corresponding to the time required for the protein concentration to reach half of its initial value, which occurs at the inflection point, and κ [1 h^{-1}] is the rate constant for fibrillization kinetics. The fibrillization assays shown as curves in Fig. 3 were created *via* regression using (12) and data from three different experimental trials (shown as symbols) for each Ω.

Fig. 3 shows that at the lowest rotation rate of $\Omega = 0.1$ rad s^{-1}, there is an increase in fibrillization kinetics (both in terms of κ and $t_{1/2}$) compared to the quiescent (non-rotating) assay. Increasing the rotation rate by a factor of ten to $\Omega = 1.0$ rad s^{-1} alters the fibrillization kinetics, although differences in the kinetics between $\Omega = 0.1$ rad s^{-1} and 1.0 rad s^{-1} are smaller than the differences between $\Omega = 0$ and 0.1 rad s^{-1}. Increasing Ω to 10.0 rad s^{-1} only produces a slight decrease in fibrillization time and a slight increase in the rate. The curve fits in Fig. 3 are reproduced in Fig. 4, where they are presented in the same plot for ease of comparison. Fig. 4 suggests that the barrier to fibrillization is overcome with a small amount of shear. Fig. 3 shows that the fibrillization kinetics accelerate as Ω is increased up to about 10 rad s^{-1}. Extracting $t_{1/2}$ and κ from the curve fits and plotting them as functions of Ω shows that they vary logarithmically with Ω. Specifically, Fig. 5(a) shows the variation of $t_{1/2}$ with rotation rate Ω, demonstrating that even at the slowest rotation rates there is a strong correlation between increased fibrillization rates and the application of flow: the

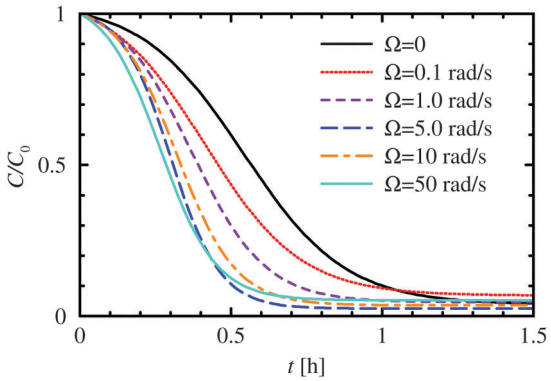

Fig. 4 The sigmoidal curve fits from Fig. 3 are shown here together for ease of comparison.

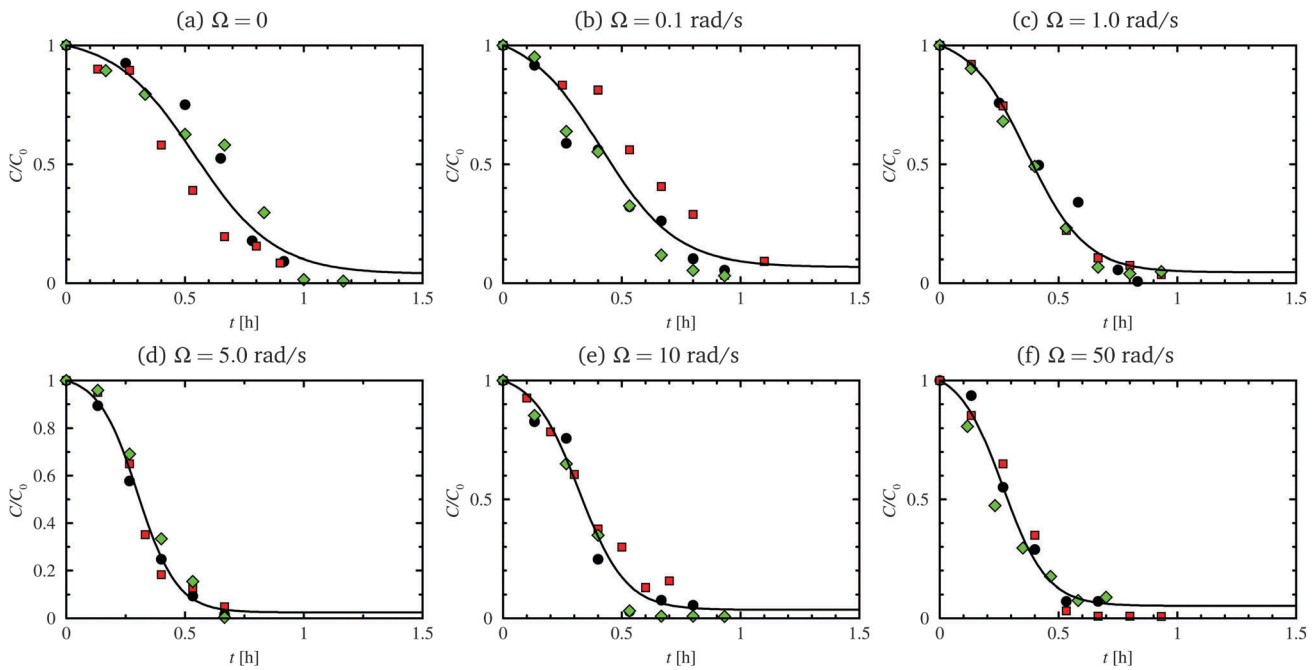

Fig. 3 Soluble protein concentration, normalized with the initial concentration, as a function of time for Ω as indicated. Three sets of experiments (symbols) were run for each Ω, and the data were for sigmoidal curves.

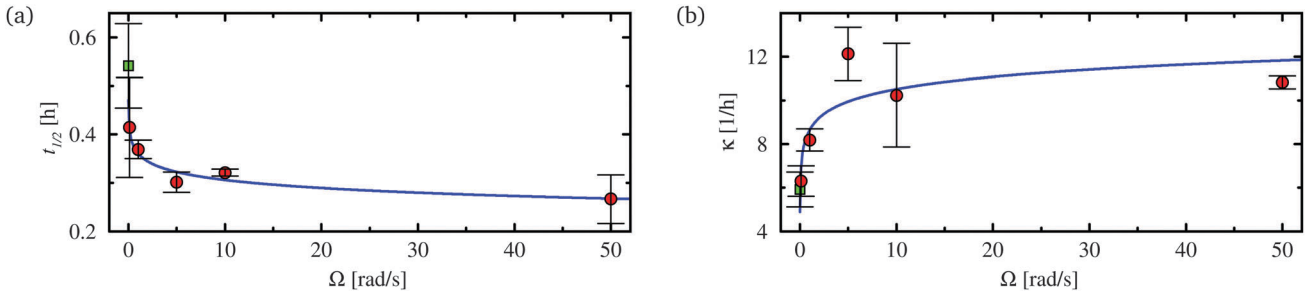

Fig. 5 Half time as a function of the rotation rate, Ω [rad s^{-1}]. The curve in (a) is a logarithmic fit to the data described by $t_{1/2} = 0.361 - 0.055 \log_{10} \Omega$, and in (b) the fit is $\kappa = 8.639 + 1.878 \log_{10} \Omega$. The square (green) symbol in each plot corresponds to $\Omega = 0$.

stronger the flow, the faster the fibrillization rate. This however is not a linear relationship. As demonstrated by the curve fit in Fig. 5(a), the half time displays a logarithmic trend with increasing Ω. The logarithmic trend also holds for the rate constant κ, plotted in Fig. 5(b), also showing that fibrillization kinetics generally increase with higher Ω.

3.2 Numerically determined flow field and shear distribution

Couette flows with a rotating outer cylinder are often used for shear investigations because they tend to have nearly uniform shear in cases where the annulus length is large compared to the gap (reducing end effects), and when the ratio of radii of the two cylinders approaches one (reducing curvature effects). In this double limit, Couette flow is the closest physically achievable approximation to uniform shear flow. However, in many laboratory experiments, such as the ones reported here, practical considerations limit the extent to which these limits can be approached, thus the shear is not uniform in either the axial or radial directions.

The flow is driven away from the idealized uniform shear by endwall effects. The primary culprit in the present geometry, where we have an open top, is the corner where the stationary inner cylinder meets the rotating bottom endwall. There is a discontinuity at this corner, where the azimuthal velocity at $r = r_i$ jumps from $v = 0$ to $v = \varepsilon$. It is from this corner that most of the vortex lines (contours of rv) enter the flow and terminate at the top surface. Even with a large aspect ratio ($h/d \gg 1$), it is impossible to prevent the bottom boundary layer from contributing end effects.

The vortex lines, streamlines, azimuthal vorticity and shear for Re values corresponding to the experimental Ω values shown in Fig. 6 indicate that even at very low rotation rates, nonlinearities induced by end effects propagate and contribute to the overall shear distribution. At a very low Reynolds number there is a large variation in radial and axial directions near the bottom. In the top three quarters of the annulus, the shear is almost uniform in both directions. As the Reynolds number increases, the region of axial invariance becomes larger so that axial variations are confined to thin boundary layers at the bottom and at the top. However, while axial invariance is gained throughout most of the flow, the radial non-uniformity grows with increasing Reynolds number.

Fig. 7 shows the radial profiles of the shear at mid-height, $S_m(r) = S(r,h/2d)$, for various Re values. The shear profiles at Re = 15 and 150 are almost uniform, closely resembling the shear profile that is generally expected from idealized rotating Couette flow (where endwall and curvature effects are absent). As the rotation rate is increased, nonlinearities due to end effects give rise to non-uniform radial profiles of shear. This is noteworthy given that experimental values of the apparent rate constant, κ, and of the kinetic half-time, $t_{1/2}$, both undergo steep transition in the range of Re = 0 to 100, while for Re $\gtrsim$ 150 both $t_{1/2}$ and κ only vary slowly (logarithmically) with Re.

One interesting aspect of Fig. 7 is that the shear at the inner and outer cylinder walls is very different, with the difference increasing with Re. Values at the inner cylinder are generally more variable than the values at the outer cylinder. Fig. 8 shows S_m *versus* Re at each cylinder wall. For Re $\lesssim$ 150, the flow is in the linear Stokes flow regime where viscous diffusion dominates and the secondary meridional flow is negligible. For Re $\gtrsim$ 150, nonlinear inertial effects start to dominate, and the secondary flow is no longer negligible and drives the shear away from being almost radially uniform to being increasingly concentrated in the inner cylinder boundary layer as Re is increased. This effect is relatively slow; Fig. 8 shows that the inner cylinder wall shear increases logarithmically with Re and that the outer cylinder wall shear decreases logarithmically with Re.

The nondimensional shear S can be made dimensional by multiplying by Ω. In the viscous dominated regime (Re $\lesssim 10^2$), $S \approx 1$ and so the dimensional shear rate is approximately equal to Ω [rad s^{-1}], and is nearly uniform throughout the flow. In contrast, in the inertia dominated regime (at higher Re), the secondary flow drives the shear away from being uniform and is significantly enhanced in the inner cylinder boundary layer, and is driven toward zero elsewhere with increasing Re.

The secondary meridional flow can be characterized by the radial profile of the axial (vertical) velocity component at the mid-height, $w_m(r) = w(r,h/2d)$. Profiles of w_m at various Re values, corresponding to the Ω values used in the experiments, are shown in Fig. 9. At Re = 15, w_m is negligibly small, whereas for Re $\gtrsim$ 150 the magnitude of w_m is about 1% of the speed of rotation of the outer cylinder, and hardly varies with Re. The nonlinearities result in a nonzero vertical flow towards the top interface in the outer part of the annulus, and a downward

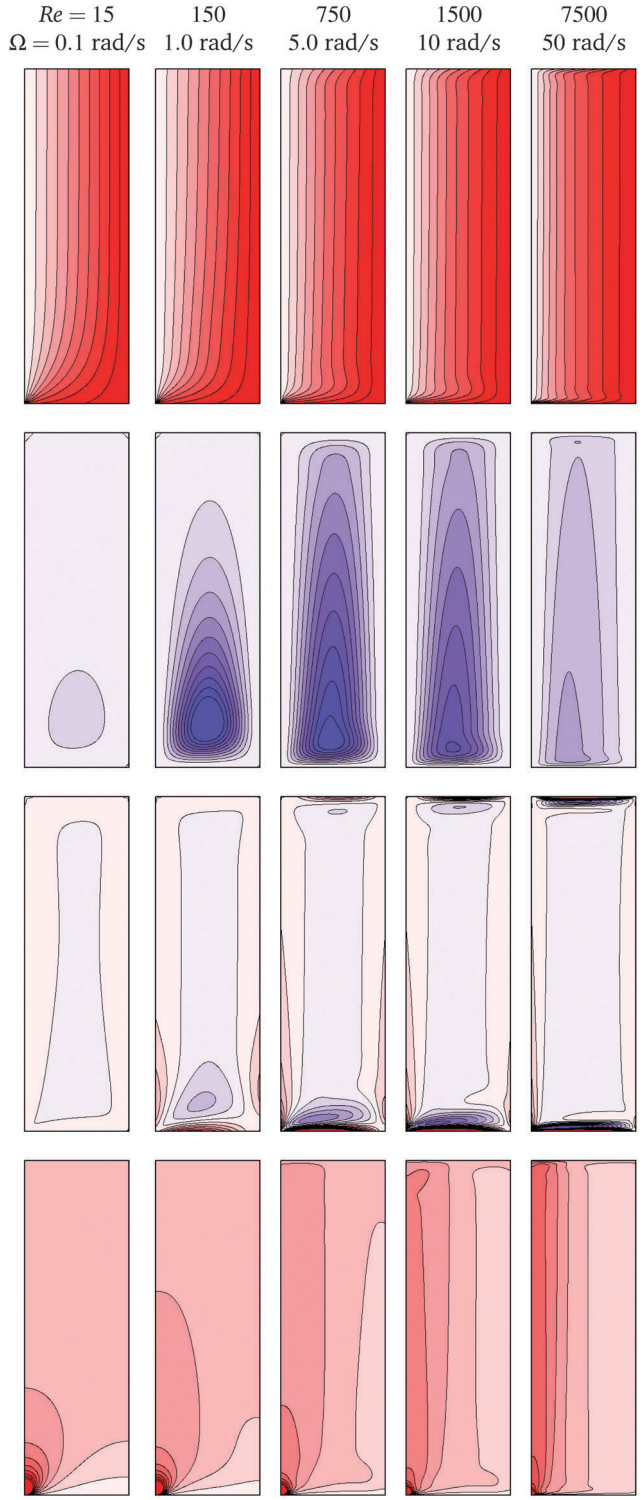

Fig. 6 Contours of the computed vortex lines rv (top row), streamlines ψ (second row), azimuthal vorticity η (third row) and shear S (bottom row) for Re (and the corresponding experimental Ω) as indicated. There are 10 levels in the ranges $rv \in [0, r_o]$, $\psi \in [-0.05, 0]$, $\eta \in [-1.0, 1.0]$, and $S \in [0, 30]$.

return flow in the inner part. Converting all quantities into dimensional form, the secondary flow magnitude increases roughly linearly with the outer cylinder rotation rate.

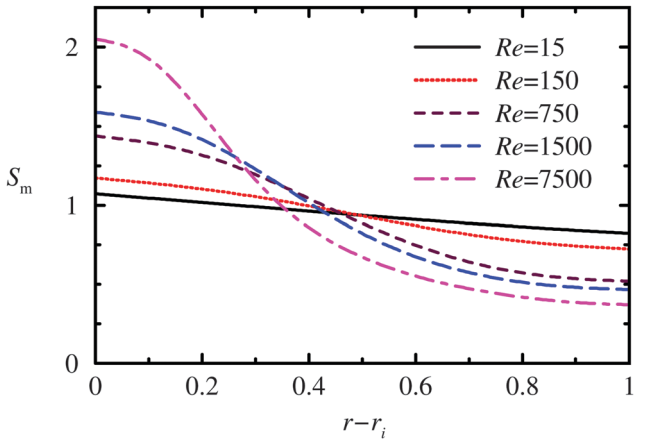

Fig. 7 Radial profiles of the shear at mid-height, S_m, for Re as indicated.

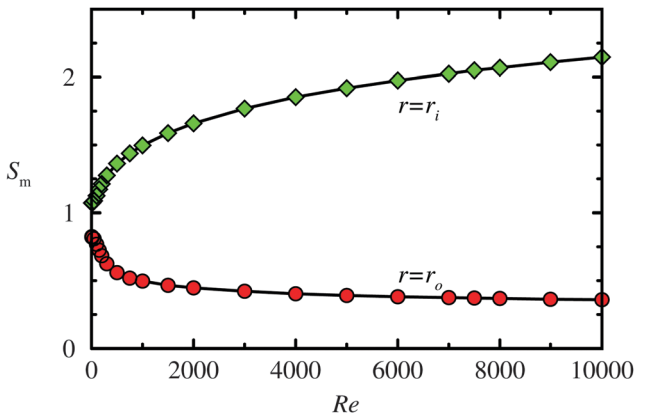

Fig. 8 Shear on the inner and outer cylinder walls at mid-height as a function of Re.

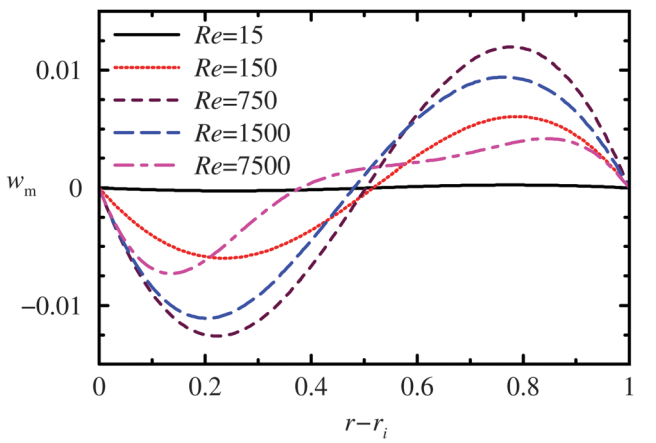

Fig. 9 Radial profiles of the axial velocity at mid-height, w_m, for Re as indicated.

4 Discussion and conclusions

The threshold for the level of shear required for significant fibrillization enhancement was experimentally found to coincide with the onset of nonlinear inertial effects in the flow. The combined effects of inertia and the bottom endwall result in a secondary

meridional flow, transporting protein solution to and from the bulk and the top hydrophobic interface. In the inertial regime, the magnitude of the secondary flow is only on the order of 1% of the azimuthal flow. However, it may be the combined effects of these two relatively weak processes – primary shearing flow and weak secondary flow transporting fluid to and from the interface – that is necessary for the accelerated fibrillization.

The presence of the top hydrophobic interface is essential for the observed fibrillization enhancement. Many previous reports have emphasized the importance of hydrophobic interfaces in shear-induced fibrillization.[9,17,18,23] Protein tertiary bonds are too strong to be torn by the levels of shear in the current experiment, however, the surface tension associated with the hydrophobic interface has a force that is large compared to the force required to unfold proteins.[9,24] This is further supported by experiments within capillary devices in which protein solutions are exposed to high shear forces but not hydrophobic interfaces.[12] In those experiments, little to no protein transformation was observed despite the large shear. High shear regimes are thought to replenish the protein at hydrophobic interfaces, resulting in the adsorption of buried hydrophobic residues to the interface. This causes rapid transition from native to denatured states at hydrophobic interfaces.[9,25,26] Although the hydrophobic interfacial area in the present study is relatively small, the secondary flow allows for more protein to access it than would otherwise be possible in a quiescent system.

Although the Navier–Stokes (continuum) modeling of the flow field is independent of the protein, it serves to illustrate a crucial point about flow-induced fibrillization. The soluble protein as well as fibrils in the bulk are advected by the flow. The steady flow is a swirling shear flow, primarily consisting of an azimuthal component that is characterized by the vortex lines (first row of panels in Fig. 6), and a secondary meridional flow that is characterized by the streamlines (second row of panels in Fig. 6). The streamlines show that protein advected by the flow is exposed to a wide range of shear (fourth row of panels in Fig. 6). This is the case for bulk advection of solution from larger to smaller radii, but it is also particularly important when solution is advected past the vicinity of the corner region where the bottom endwall and the inner cylinder meet. In this region the variation in shear is very large and most of the bulk fluid (and dissolved protein) is transported through it. This creates a situation in which a steady flow advects the protein and subjects it to large variations in shear. The detailed time histories of the shear to which protein is subjected to coming from the continuum hydrodynamics may provide essential information for, say, molecular dynamics simulations which may be used to probe the microscopic processes involved in shear induced fibrillization. Furthermore, the large variation in shear near the corner may provide an additional mechanism of protein denaturation which is not considered by the typical assumption of uniform shear attributed to Couette geometries.

Acknowledgements

We thank Dmitri Zagorevski for performing the mass spectrometry analysis presented in the ESI.† This work was supported by NASA under grant NNX13AQ22G.

References

1 C. Dobson, *Trends Biochem. Sci.*, 1999, **24**, 329–332.
2 R. N. Rambaran and L. C. Serpell, *Prion*, 2008, **2**, 112–117.
3 L. Nielsen, R. Khurana, A. Coats, S. Frokjaer, J. Brange, S. Vyas, V. N. Uversky and A. L. Fink, *Biochemistry*, 2001, **40**, 6036.
4 F. Chiti, P. Webster, N. Taddei, A. Clark, M. Stefani, G. Ramponi and C. M. Dobson, *Proc. Natl. Acad. Sci. U. S. A.*, 1999, **96**, 3590–3594.
5 S. N. Jamadagni, R. Godawat and S. Garde, *Annu. Rev. Chem. Biomol. Eng.*, 2011, **2**, 147–171.
6 D. M. Ridgley, E. C. Claunch, P. W. Lee and J. R. Barone, *Biomacromolecules*, 2014, **15**, 1240–1247.
7 D. F. Waugh, D. F. Wilhemson, S. L. Commerford and M. L. Sackler, *J. Am. Chem. Soc.*, 1953, **75**, 2592–2600.
8 R. Crespo, F. A. Rocha, A. M. Damas and P. M. Martins, *J. Biol. Chem.*, 2012, **287**, 30585–30594.
9 I. B. Bekard, P. Asimakis, J. Bertolini and D. E. Dunstan, *Biopolymers*, 2011, **95**, 733–745.
10 D. E. Dunstan, P. Hamilton-Brown, P. Asimakis, W. Ducker and J. Bertolini, *Protein Eng., Des. Sel.*, 2009, **22**, 741–746.
11 E. K. Hill, B. Krebs, D. G. Goodall, G. J. Howlett and D. E. Dunstan, *Biomacromolecules*, 2006, **7**, 10–13.
12 J. Jaspe and S. J. Hagen, *Biophys. J.*, 2006, **91**, 3415–3424.
13 P. Szymczak and M. Cieplak, *J. Chem. Phys.*, 2007, **127**, 1551061.
14 D. Posada, P. M. Tessier and A. H. Hirsa, *Biotechnol. Bioeng.*, 2012, **109**, 840–845.
15 S. A. McBride, C. F. Tilger, S. P. Sanford, P. M. Tessier and A. H. Hirsa, *J. Phys. Chem. B*, 2015, **119**, 10426–10433.
16 C. Akkermans, P. Venema, S. S. Rogers, A. van der Goot, R. M. Boom and E. van der Linden, *Food Biophys.*, 2006, **1**, 144–150.
17 J. Pronchik, X. He, J. T. Giurleo and D. S. Talaga, *J. Am. Chem. Soc.*, 2010, **132**, 9797–9803.
18 L. Jean, C. F. Lee, C. Lee, M. Shaw and D. J. Vaux, *Philos. Trans. R. Soc., A*, 2010, **24**, 309–317.
19 G. I. Taylor, *Proc. R. Soc. London, Ser. A*, 1923, **104**, 213–218.
20 C. C. Lee, A. Nayak, A. Sethuraman, G. Belfort and G. J. McRae, *Biophys. J.*, 2007, **92**, 3448–3458.
21 S. A. McBride, MSc thesis, Rensselaer Polytechnic Institute, 2015.
22 J. E. Young, D. Posada, J. M. Lopez and A. H. Hirsa, *Soft Matter*, 2015, **11**, 3618–3628.
23 P. D. Virkar, T. J. Narendranathan, M. Hoare and P. Dunnill, *Biotechnol. Bioeng.*, 1981, **23**, 425–429.
24 R. B. Best, D. J. Brockwell, J. L. Toca-Herrera, A. W. Blake, D. A. Smith, S. E. Radford and J. Clarke, *Anal. Chim. Acta*, 2003, **479**, 87–105.
25 A. K. Buell, A. Dhulesia, D. A. White, T. P. J. Knowles, C. M. Dobson and M. E. Welland, *Angew. Chem., Int. Ed.*, 2012, **51**, 5247–5251.
26 B. L. Talboys and P. Dunnill, *Biotechnol. Bioeng.*, 2004, **27**, 1730–1734.